

Magnetic Perturbation Diagnostics in the High-Temperature, Lithiated Environment of LTX- β [v1-2]^{a)}

P E Hughes,^{1, b)} R Majeski,¹ R Kaita,¹ T Kozub,¹ C Hansen,² and D P Boyle¹

¹⁾Princeton Plasma Physics Laboratory, Princeton, NJ 08543, USA

²⁾Department of Aeronautics & Astronautics, University of Washington, Seattle, WA 98195 USA

(Dated: 13 April 2018)

Magnetic perturbation measurements will be invaluable for characterizing Lithium Tokamak Experiment Beta (LTX- β) plasmas due to the time-evolving, 3D nature of the magnetic fields generated by eddy currents in the vessel and copper shell segments, as well as enhanced MHD instability drive due to newly introduced neutral beam heating. The LTX- β upgrade includes two new arrays of Mirnov coils: a shell eddy sensor array of two-axis coils distributed over the back surface of one shell segment, and a toroidal array of poloidal field coils at the low-field side midplane gap. Evaporative lithium wall-coating and the high temperatures required for liquid lithium wall operation both complicate the implementation of in-vessel diagnostics. While the shell array is protected from lithium exposure, the shell segment to which it is mounted will at times exceed 300°C. The toroidal array, however, will experience direct line-of-sight exposure to the lithium evaporator as well as close proximity to the hot shell, and may also be subject to poorly-confined, beam-driven fast ions. We describe how the two new Mirnov coil arrays meet these environmental challenges and enhance the LTX- β diagnostic suite.

I. INTRODUCTION

The main focus of LTX has been to study the low-recycling regime expected to arise in the case of a fully-surrounding wall with a lithium plasma-facing surface¹. Retention of neutralized hydrogen in the lithium coating reduces the cold gas inventory, leading to the observation of flat electron temperature profiles² due to the absence of edge cooling. However, this regime is obviously incompatible with edge fueling by cold gas, which has relegated LTX flat- T_e experiments to a regime in which density is low and decreases in time due to a lack of fueling. The upgraded LTX- β will employ a neutral beam to provide high-energy core fueling as well as heating, which is expected to considerably increase β and the associated MHD instability drive³. However, prior LTX research and diagnostic suites have not focused on MHD stability, due partly to limited toroidal resolution⁴. At the same time, a sophisticated understanding of LTX- β plasmas will require faithful, high-quality equilibrium reconstructions, which have been made challenging in the past due to the time-evolving, non-axisymmetric eddy current fields of the LTX plasma-facing shell^{5,6} (Fig. 1).

In order to resolve these physics diagnostic challenges, in addition to an expansion of the re-entrant Mirnov coil array from 18 orthogonal Mirnov coil triplets to 28 triplets⁴, two new Mirnov coil arrays will be implemented in LTX- β . A toroidal array (TA) of 10 poloidal field Mirnov coils installed at the low-field side midplane will

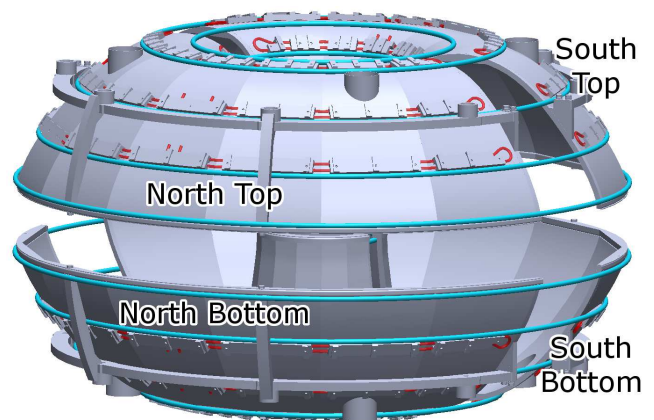


FIG. 1. A CAD rendering of the four LTX stabilizing shell segments, arranged in north and south top/bottom pairs. Each shell segment is composed of seven 3/8"-thick sheets of copper, explosively bonded to 1/16"-thick 304 stainless steel on the plasma-facing side, and welded together. Each shell weld corresponds to the toroidal position of a toroidal field magnet. The low-field side poloidal gap is ≈ 5 " across, and both toroidal gaps are 22.5° wide.

allow the identification of non- $n = 0$ structures up to $n = 4$ with high fidelity, extending LTX- β 's ability to resolve non-axisymmetric perturbations. Also, a Shell Eddy Sensor Array (SESA) of 14 Mirnov coils in shell-perpendicular and shell-tangent pairs mounted to the back of one shell segment will provide a more detailed, time-resolved picture of the patterns of eddy currents flowing through the shells. Considerable improvements to LTX equilibrium reconstructions were observed by modeling the eddy currents of both the vessel and shell, and introducing the axisymmetric projection of the first eigenmode of each to the reconstruction⁷. A direct mea-

^{a)}Contributed paper published as part of the Proceedings of the 22nd Topical Conference on High-Temperature Plasma Diagnostics, San Diego, California, April, 2018.

^{b)}Electronic mail: phughes@pppl.gov

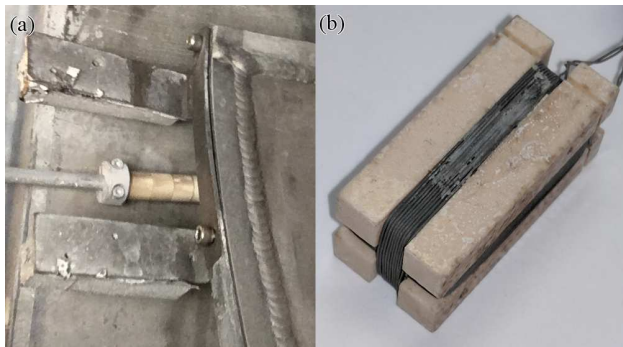


FIG. 2. The “Gap Sensors,” a poloidal array of eighteen 2-axis Mirnov coils at the west shell gap in LTX, were protected by stainless shim stock shields spot-welded to tungsten mounting tabs (a). As seen on one of the Gap Sensor Mirnov coils (b), exposure to lithium led to shorting between turns on more than half of the array. Those that survived were salvaged for use as LTX- β Shell Eddy Sensors.

surement of perturbed fields close to the shell segments will help to resolve these currents and their contribution to the measured fields still further.

II. CHALLENGES TO DIAGNOSTICS IN LTX- β

The lithium-saturated, high-temperature environment inside LTX- β represents a special threat to in-vessel diagnostics such as Mirnov coils. The high temperature ($\sim 350^\circ\text{C}$) of the plasma-facing shell segments and the demands placed on vacuum quality due to the reactivity of liquid lithium compel the use of ceramics rather than plastics. Further, liquid lithium is an exceptionally aggressive, invasive substance, attacking nearly all materials to some degree, although copper and most ceramics—the typical materials used in the construction of Mirnov coils for high-temperature applications—are particularly vulnerable⁸.

The LTX- β upgrade effort included the removal of a number of Mirnov coils which had been rendered inoperable, or whose performance had been altered in-situ by lithium infiltration. Figure 2a shows a segment of the “Gap Sensor” array: a set of 18 two-axis Mirnov coils protected by a shim stock shield spot-welded to a tungsten mounting plate⁹. Most of these sensors still suffered considerably from lithium exposure, however, as seen in Fig. 2b, where lithium infiltration (light gray) into the magnesia (MgO) wire insulation (dark gray) can be seen. Note that the yttria-magnesia ($\text{Y}_2\text{O}_3\text{-MgO}$) mandrel has relatively good resistance to lithium infiltration, but yttria is not commonly available as cable insulation.

Fig. 2a also shows one of sixteen shell-mounted flux loops protected by a stainless steel tube and insulated from the shell by steatite ($\text{SiO}_2\text{-MgO}$) and yttria-magnesia beads⁹. Several of these flux loops were repaired with fiberglass insulation to keep their shield tubes



FIG. 3. The “In-Shell Sensors”, a set of three toroidally-discrete poloidal arrays of 10 sensors each, able to distinguish $n = 1$ and $n = 2$ structures. The tubes were infiltrated by creeping liquid lithium, disabling the Mirnov coils.

electrically isolated.

Another set of Mirnov coils, the “in-shell” arrays, were protected within stainless steel tubes⁶. Each LTX shell segment was constructed of seven segments, and the in-shell Mirnov coil tubes were positioned inside the poloidal grooves where segments were welded together (Fig. 3). Although protected from direct lithium exposure, hot liquid lithium is able to creep over surfaces and through narrow spaces. The heating of the shell segments permitted lithium to infiltrate the in-shell tubes, disabling the Mirnov coils.

Improvements to the lithium evaporation systems in LTX- β will only increase lithium coverage, requiring rigorous prevention of both line-of-sight deposition and creeping access. These challenges are addressed differently for each of the two new arrays.

III. SHELL EDDY SENSOR ARRAY

Although modeling has been performed to calculate the dominant eddy current eigenmodes of the vessel and shell, the only recent measurements have been from the no longer functional gap sensor array overhanging the west edge of the northern top/bottom shell segment pair. The new Shell Eddy Sensor Array (SESA) is mounted to the north top shell segment, probing both the east and west edges (EE and WE), as well as east/west upper (EU/WU) and midplane (EM/WM), and a north midplane (NM) pair at the toroidal center of the shell segment. Each location houses a two-axis Mirnov coil pair identical in design to the gap sensors (Fig. 2b), with one coil perpendicular to and the other coil tangent to the shell surface. Each Mirnov coil pair is mounted to a 1/16” thick 316 SAE stainless steel bracket by a pair of screws (lubricated with boron nitride powder as a vacuum-safe anti-sieze), and covered by a 0.003” thick 316 shim stock electrostatic shield spot-welded to the

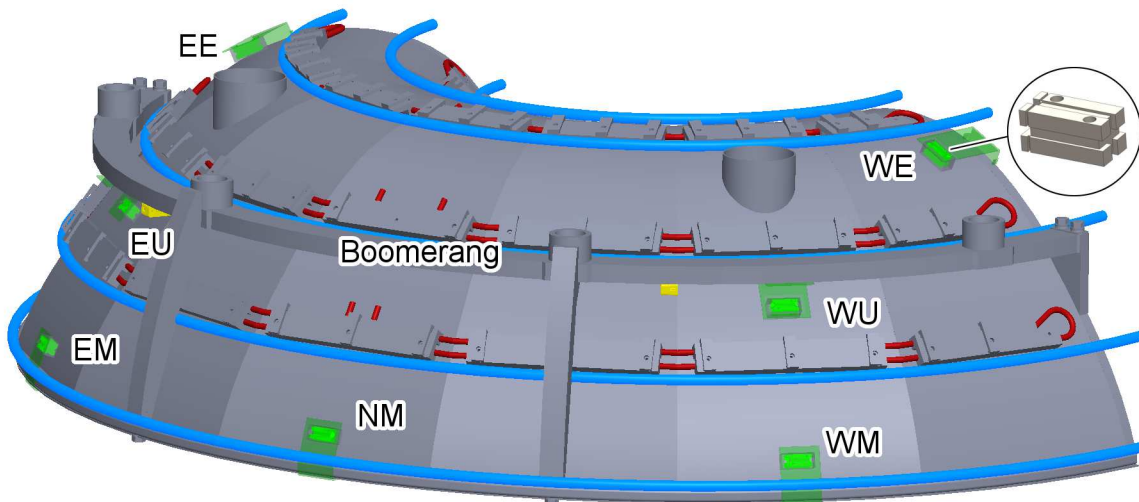


FIG. 4. CAD drawing of Shell eddy sensors mounted to back of North Upper shell segment. Shell eddy sensor brackets in transparent green show how sensors are mounted to the shell segment at the edges, at the midplane, and below the shell support “boomerang.” Sensor forms are shown in bright green to indicate orientation, and ceramic D-Sub connectors where the leads are bundled before continuing on to the feedthrough are shown in yellow. Also shown are the flux loops blue, and the shell heater tubes (red) can be seen between their mounting fixtures.

bracket. Since the predicted eddy currents used in the PSI-Tri code are mostly toroidal at the toroidal center of each shell segment⁷, the central five SESA Mirnov coil pairs are oriented to pick up poloidal and radial field components (Fig. 4). The remaining two pairs are oriented to measure vertical and toroidal fields from eddy currents flowing poloidally at the shell segment edges.

The SESA avoids lithium exposure mainly by the advantage of its placement. Placed behind the shell, there will be no line-of-sight to the lithium evaporator, and the SESA Mirnov coils’ distance from the shell segment edges ($> 1''$) reduces the danger of lithium creep. Installation on the upper shell segment also avoids exposure to any excess lithium dripping or flowing downward from the midplane or toroidal shell gaps. All cable runs are kept well clear of the midplane gap, and close to the shell support “boomerang,” near the third flux loop above the midplane. To simplify installation in-vessel, the east and west halves are each routed through a ceramic D-sub connector mounted below the “boomerang” (marked yellow in Fig. 4) to the feedthrough. Due to its proximity and limited access, the north-midplane Mirnov coil pair is cabled directly to the feedthrough.

The SESA is constructed from the repurposed surviving Mirnov coil pairs of the gap sensor array, as well as one spare two-coil probe that was never in vessel. The yttria mandrel and magnesia wire insulation can tolerate temperatures in excess of 2000°C , making them among the most temperature-resistant materials in LTX- β . However, the extreme abrasiveness of the magnesia insulation introduced additional challenges during installation. Each coil’s leads had been twisted into pairs, and the two pairs were run in a single electrostatic shield braid. Several intermittent coil-to-coil shorts were dis-

covered during installation due to each twisted pair’s insulation abrading through the other. The problem was resolved by adding a fiberglass sleeve to each twisted pair running the full length from the mandrel to the in-vessel connector, and each shield braid was spot-welded to the bracket for strain relief. To prevent unraveling of the fiberglass, the end of each sleeve was wetted with “Fort-a-fix” high-temperature ceramic cement. To avoid these difficulties of working with magnesia-insulated wire, cabling from the east and west D-sub to the feedthrough connector was run with bare copper clad in fiberglass sleeving and twisted into pairs.

IV. MIDPLANE TOROIDAL ARRAY

Other than the short-lived in-shell Mirnov coils (Fig. 3), LTX has not previously had the capability of resolving toroidal field structures besides the $n = 0$ component and local variations at a single toroidal location. In addition to β -driven MHD modes which could potentially be destabilized by LTX- β ’s increased power and neutral beam, the introduction of a toroidal array will provide the ability to assess low- n (i.e. $n < 5$) non-axisymmetries of the equilibrium^{4,7}. This might be caused, for example, by plasma response to shell eddy currents, or non-axisymmetric vessel eddy currents. As seen in Fig. 5, interference from the dump plate of the neutral beam located at the LFS midplane under magnet K, the geometry of other diagnostics, and a desire to install Mirnov coils in diametric pairs all constrained the distribution of the toroidal array.

Installed at the LFS midplane, every TA Mirnov coil position will have direct line-of-sight exposure to lithium

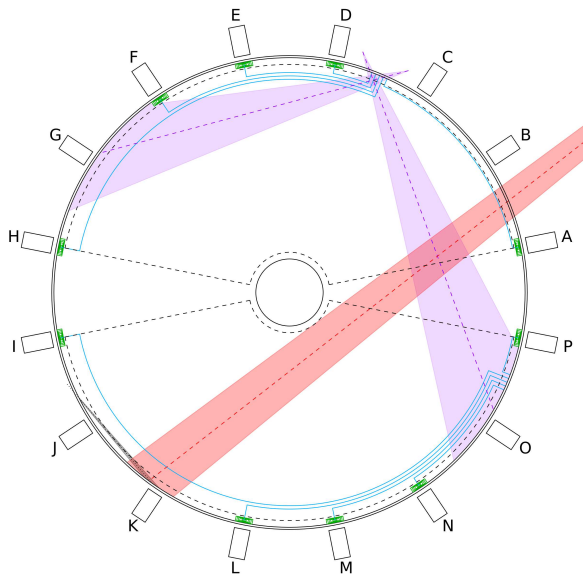


FIG. 5. Overhead view of the arrangement of toroidal array Mirnov coils (green). Certain locations were unavailable, such as locations **J** near the edge D_α chord (gray), **K** which houses the dump plate for the neutral beam (red), and **G** and **O** at the center of the co-rotation and background ChERS views. To avoid crossing the gaps between shells (dashed black) where in-vessel cabling (blue) would be exposed to lithium, leads from Mirnov coils **A** through **H** are run to a feedthrough at bay C-D, and from Mirnov coils **I** through **P** are run to a feedthrough at bay O-P.

evaporation. Additionally, once the neutral beam begins operating, there will be a risk of poorly-confined fast ions escaping through the midplane gap, requiring a heat shield of some strength, but to avoid losing Mirnov coil sensitivity, the shield cannot form a circuit about the coil's axis. Finally, although the vessel wall will not be deliberately heated, it will be radiatively heated by the shells. Due to the lack of secure mounting points on the inside of the vessel, the quality of heat sinking is difficult to estimate, so all materials in the TA sensor assemblies still must be good for high vacuum at least to $\sim 350^\circ\text{C}$.

To resolve these assorted challenges, the TA employs coils wound in bare copper on Macor mandrels (good to $\sim 800^\circ\text{C}$) and insulated with Omegabond 700 (specified for $\leq 871^\circ\text{C}$) high-temperature cement at the mandrel¹⁰ and fiberglass insulation ($\sim 650^\circ\text{C}$) sleeved individually on each lead, well within thermal and vacuum quality tolerance, but requiring robust lithium protection. As with the SESA, all fiberglass sleeve ends were wetted with ceramic cement to prevent fraying. A mounting bracket (Fig. 6a) is positioned with a custom jig that provides a toroidal and vertical reference, and spot-welded to the vessel wall by shim stock tabs at each toroidal position, with the open end of the bracket downward. Each coil is fixed by screws to a mounting plate with a vertical gap in the center, allowing the Mirnov coil leads to exit the back of the plate. An electrostatic

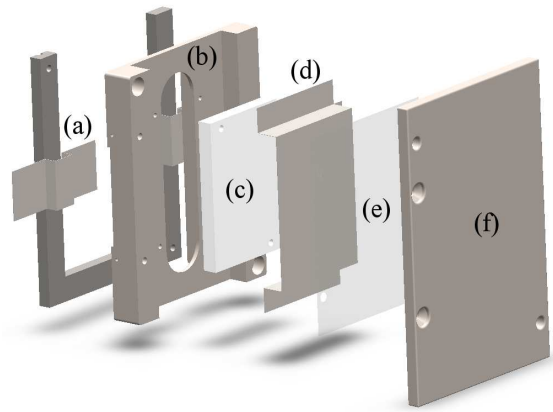


FIG. 6. Exploded view of the toroidal array assembly. From right to left: a. mounting bracket, b. mounting plate, c. 1D Mirnov coil, d. electrostatic shield, e. mica insulator, and f. heat shield. When the heat shield is installed, it holds the mounting screws captive in counter-bored spaces within the mounting plate, while providing access for a hex key. This avoids the handling of small parts in-vessel, simplifying the installation procedure.

shield is spot-welded over the Mirnov coil, blocking most of the lithium line-of-sight, but open on one side to impact on Mirnov coil sensitivity. The heat shield (Fig. 6f) fastens to the mounting plate at the side on which the electrostatic shield is open, closing off the line-of-sight completely providing protection from fast ions, but does not contact the mounting plate on the opposite side. A 0.001" mica sheet separates the heat shield from the electrostatic shield to avoid making an unwanted circuit. The back of the mounting plate makes a close seal to its bracket, protecting the Mirnov coil leads from the top and both sides.

Mirnov coil leads are passed down steel tubes extending 10" below the midplane (13" below at the **toroidal edges of the shell segment** where there is less protection from lithium exposure), and 304 SAE steel braid provides electrostatic shielding on the run to the feedthroughs. To ensure protection from lithium exposure, braid-covered cable runs never cross shell gaps, but stay behind the shell at which the originated, and exit at ports below the midplane (Fig. 5, blue lines). All metal parts are 316 SAE for lithium resistance and minimal magnetic susceptibility unless otherwise stated. Due to the use of #0 and #2 screws, they were silver-plated to prevent galling.

V. CALIBRATION AND ANALYSIS

Calibration of the TA and SESA was performed with the use of a $R = 3.5''$ Helmholtz coil designed specifically for the calibration of small ($L < 1''$) Mirnov coils. The Helmholtz coil was first calibrated against a precision commercial magnetometer using a DC supply, and found

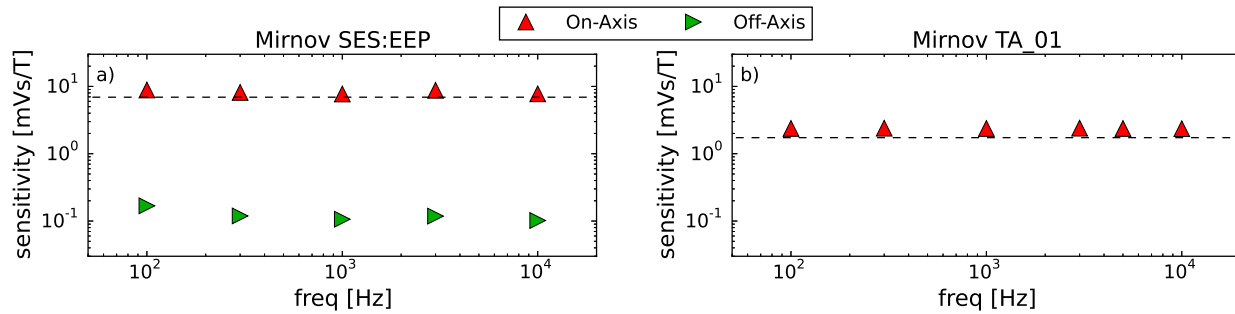


FIG. 7. On-axis calibration data (\triangle) for a Shell Eddy Sensor (a), and a Toroidal Array sensor (b), relative to calculated sensitivity (dashed line) in mVs/G, related to effective NA. The Shell Eddy Sensor show here is at the East Edge position, Perpendicular to shell (EEP), and the Toroidal Array sensor is located at magnet A. Due to the Shell Eddy Sensor's mounting plate, there is a non-zero pickup of off-axis fields (\triangleright). Greater than predicted sensitivity suggests the effective flux area larger than that used in the calculation. Sensitivities are typical.

to provide $1.15 \pm 0.03\text{G/A}$. Mirnov coil calibrations were carried out by energizing the Helmholtz coil, originally with a high-power, wide-band amplifier, and later with a commercially available audio amplifier driven by a digital function generator. Measuring current into the Helmholtz with a Pearson current transformer yielded B at the driving frequency, and using this to normalize integrated Mirnov coil signal yielded Vs/T-equivalent to an effective NA .

Typical results for SESA and TA Mirnov coils calibrated by multiple, discrete sine wave measurements are shown in Fig. 7. Off-Axis pickup on SESA Mirnov coils (green triangles) varies with mounting plate geometry, and can climb as high as 20% of On-Axis signal (red triangles) at high frequencies when the mounting plate supports significant eddy currents. Another technique employing a single square wave has also been employed, but while square wave decomposition is a much faster technique to perform, the rapid loss of SNR at higher frequencies leads to poor precision above 3kHz. Using the multiple, discrete sine wave method, the mean SESA sensitivity is $9.48 \pm 0.55\text{mVs/T}$ ($\pm 5.8\%$), and the mean TA sensitivity is $2.38 \pm 0.02\text{mVs/T}$ ($\pm 0.8\%$). Both of these results are somewhat higher than predicted from specified dimensions. Assuming the magnetometer to which the Helmholtz was calibrated at DC was precise to within $\pm 0.3\text{G}$, this is most likely due to coils bulging outward from their nominal dimensions on the their mandrels.

VI. SUMMARY AND EXPECTATIONS

Two new magnetic diagnostic sets have been implemented in the high-temperature, liquid lithium saturated environment of LTX- β . Each array employs different tactics to maximize diagnostic survivability under hostile conditions, building on lessons learned from previous diagnostics. The addition of arrays designed for studying non-axisymmetric and eddy current

fields will open up a new avenue for investigating the behavior of the novel flat-temperature profile regime with the heating, fueling, and confinement upgrades underway for LTX- β . Well-optimized reconstructions aided by an enhanced magnetics suite will be a critical basis for understanding the lithiated wall's effects on plasma-material interaction, recycling, and confinement.

ACKNOWLEDGMENTS

The authors wish to thank G. Smalley, K. Lamb, J. Armeli, and F. Rabanales for technical support. This work was supported by U.S. DOE contract numbers DE-AC02-09CH11466 and DE-AC05-00OR22725.

- ¹S. I. Krasheninnikov, L. E. Zakharov, and G. V. Pereverzev, *Physics of Plasmas* **10**, 1678 (2003), <https://doi.org/10.1063/1.1558293>.
- ²D. P. Boyle, R. Majeski, J. C. Schmitt, C. Hansen, R. Kaita, S. Kubota, M. Lucia, and T. D. Rognlien, *Phys. Rev. Lett.* **119**, 015001 (2017).
- ³R. Koch, *Fusion Science and Technology* **45**, 183 (2004), <https://doi.org/10.13182/FST04-A482>.
- ⁴J. C. Schmitt, J. Bialek, S. Lazerson, and R. Majeski, *Review of Scientific Instruments* **85**, 11E817 (2014), <https://doi.org/10.1063/1.4892159>.
- ⁵L. B. Hopkins, J. Menard, R. Majeski, D. Lundberg, E. Granstedt, C. Jacobson, R. Kaita, T. Kozub, and L. Zakharov, *Nuclear Fusion* **52**, 063025 (2012).
- ⁶L. Berzak, A. D. Jones, R. Kaita, T. Kozub, N. Logan, R. Majeski, J. Menard, and L. Zakharov, *Review of Scientific Instruments* **81**, 10E114 (2010), <https://doi.org/10.1063/1.3484488>.
- ⁷C. Hansen, D. P. Boyle, J. C. Schmitt, and R. Majeski, *Physics of Plasmas* **24**, 042513 (2017), <https://doi.org/10.1063/1.4981214>.
- ⁸D. W. Jeppson, J. L. Ballif, W. W. Yuan, and B. E. Chou, "Lithium literature review: Lithium's properties and interactions," *Tech. Rep. 15* (Hanford Site (Wash.), 1978).
- ⁹L. Berzak, *Plasma Start-up in a Spherical Tokamak with Close-fitting Conducting Walls*, Ph.D. thesis, Princeton University (2010).
- ¹⁰S. P. Gerhardt, K. Erickson, R. Kaita, J. Lawson, R. Mozulay, D. Mueller, W. Que, N. Rahman, H. Schneider, G. Smalley, and K. Tresemer, *Review of Scientific Instruments* **85**, 11E807 (2014), <https://doi.org/10.1063/1.4889781>.